Thin-Walled Structures 189 (2023) 110853

Contents lists available at ScienceDirect

Thin-Walled Structures

journal homepage: www.elsevier.com/locate/tws

Full length article

Polyaspartic polyurea/graphene nanocomposites for multifunctionality: Self-healing, mechanical resilience, electrical and thermal conductivities, and resistance to corrosion and impact

Qingshi Meng [a,1], Peng Wang [a,1], Yin Yu [b], Jianbang Liu [c], Xiao Su [d], Hsu-Chiang Kuan [e,*], Baozhu Wang [f], Liqun Zhang [g], Yingyan Zhang [h], Dusan Losic [i], Jun Ma [d,*]

[a] College of Aerospace Engineering, Shenyang Aerospace University, Shenyang 110136, China
[b] College of Medicine and Bioinformatics Engineering, Northeastern University, Shenyang 110819, China
[c] College of Civil Aviation, Shenyang Aerospace University, Shenyang 110136, China
[d] UniSA STEM and Future Industries Institute, University of South Australia, SA 5095, Australia
[e] Department of Chemical and Materials Engineering, Southern Taiwan University of Science and Technology, Tainan City 710301, Taiwan
[f] Qingdao Airjj New Materials Co. Ltd., Qingdao 266100, China
[g] Engineering Research Center of Elastomer Materials on Energy Conservation and Resources, Ministry of Education, Beijing, 100029, China
[h] School of Engineering, RMIT University, PO Box 71, Bundoora, VIC 3083, Australia
[i] The ARC Graphene Research Hub, School of Chemical Engineering and Advanced Materials, The University of Adelaide, SA 5005, Australia

ARTICLE INFO

Keywords:
Polyaspartic polyurea
Self-healing
Graphene nanoplatelets
Multifunctionality

ABSTRACT

Polyurea elastomers have attracted increasingly more attention due to excellent mechanical performance, and their wide industrial applications are in need of multifunctionality such as thermal conductivity. We herein prepared polyaspartic polyurea elastomers with optimal tensile strength and fracture strain by adjusting the isocyanate index and free isocyanate content. As a class of nanofiller, isocyanate-modified graphene nanoplatelets (*IP*-GNPs) were developed and they formed a stable, robust interface with the polyurea matrix, resulting in mechanical reinforcement and multifunctionality. The nanocomposite at 0.05 vol% of *IP*-GNPs revealed a tensile strength of 15.72 ± 0.67 MPa, representing an increment of 108.21% over pure polyurea, with excellent resistance to acidic and alkali corrosion. After 9 h of post-maintenance at 60 °C, the nanocomposite reached a healing efficiency up to 80.10% as driven by hydrogen bonds. An electrical percolation threshold was observed at 3.61 vol% of *IP*-GNP for the nanocomposites. The thermal conductivity reached 38.49 W/m K at 7.00 vol% due to the formation of the *IP*-GNP network in polyurea, where the electron thermal conductivity plays a dominant role. In comparison with those high thermal conductivity values obtained by back-filling polymers into a network established beforehand, this facile approach would be highly favored in industry for the development of elastomer nanocomposites with multifunctionality for many applications, e.g. smart sensors, protective coatings, energy harvesting, etc.

1. Introduction

Polyurea elastomers are a class of emerging macromolecules, each of which is composed of an isocyanate component (–NCO) and an amino component ($–NH_2$); these two components react to produce a urea group [1]. A polyurea macromolecule consists of soft and hard segments. The soft segments consisting of amino compounds can readily change their conformations, to provide polyurea not only with high elasticity and ductility but also lower glass transition temperatures than room temperature. The hard segment, isocyanate, has high glass transition temperature and is rigid, providing polyurea with high modulus and strength. The micro-phase separation in polyurea is caused by (i) the thermodynamic incompatibility between soft and hard segments and (ii) the strong hydrogen bonding between hard segments [2,3]. This morphology endows polyurea with a variety of excellent physicochemical properties. Since the extremely fast reaction rate limits the application of polyurea materials, it is of significance to improve polyurea formulations to reduce the reaction rate and make the reaction time controllable.

To improve the mechanical and functional performance of polyurea materials, a variety of fillers have been developed for polyurea nanocomposites [4–6]. Zhang et al. [7] compounded hydroxyapatite

* Corresponding authors.
E-mail addresses: hckuan@stust.edu.tw (H.-C. Kuan), jun.ma@unisa.edu.au (J. Ma).
[1] Qingshi Meng and Peng Wang contributed equally to this article.

https://doi.org/10.1016/j.tws.2023.110853
Received 9 April 2023; Received in revised form 11 May 2023; Accepted 11 May 2023
Available online 16 June 2023

as the reinforcing phase with polyurea, and the formation of hydrogen bonds between hydroxyapatite nanorods and polyurea enhanced the mechanical properties. Bordbar et al. [8] incorporated silver nanoparticles into polyurea coatings, and the resultant nanocomposite exhibited higher heat transfer rate and better corrosion resistance. Yu et al. [9] prepared a new silicone-modified polyurea coating for asphalt pavements to improve anti-icing performance. The average ice strength was reduced by 61.2%, and the coating showed good anti-icing performance even after 10 freezing-thawing cycles. Although the above efforts have improved the mechanical properties of materials or provided certain functions, multifunctional, mechanically resilient polyurea nanocomposites are in high demand in industry.

Since carbon-based materials feature exceptional mechanical robustness and electrical and thermal conductivities, these have been proposed as an ideal reinforcing phase for multifunctional composites [10–15]. Yang et al. [16] reported a low-cost, biodegradable starch/graphite composite by exploiting the cation-π interactions between ammonium ions and graphite to improve the degree of delamination as well as the dispersion of graphite in a starch matrix. Li et al. [17] used miscible poly(L-lactide) as an adjuvant and prepared polyoxymethylene (POM)/multi-walled carbon nanotube (MWCNT) composites and POM/graphene nanoplatelet (GNP) composites. MWCNTs and GNPs provided the matrices with excellent thermal conductivity, electromagnetic interference shielding, Joule heating, and anti-dripping properties. Guo et al. [18] used graphene oxide (GO) to enhance the flame retardancy of polydimethylsiloxane(PDMS) foam materials, and GO/PDMS foam composites added at only 0.04 wt% exhibited excellent flame retardancy (40.6% reduction in heat release rate and 27.1% of limit oxygen index) without affecting the low density and mechanical flexibility. Hernández et al. [19] prepared a rubber nanocomposite with excellent self-healing and electrically and thermally conductive properties by adding graphene, and investigated in-depth the effect of graphene loading on the recovery of mechanical and thermal and electrical properties.

Graphene, as the “ super star ” in engineering materials, has attracted intensive attention from scholars and industry. However, untreated graphene and graphene oxide (GO) are not ideal [20–23], because the former cannot uniformly disperse in the polymer, and the latter is limited by low structural integrity and the need for reduction to obtain desirable electrical and thermal conductivities [24,25]. Graphene nanoplatelets (GNPs) each are composed of few-layer graphene and their mechanical properties and electrical and thermal conductivities are close to single-layer graphene. More importantly, GNPs contain a low proportion of oxygen-containing groups such as epoxide groups which can be used to form a strong interface with polymer matrices. However, the current preparation methods for many polymer/GNP nanocomposites are in need of organic solvents, which are not environmentally friendly. The mechanochemical treatments for polymer nanocomposites has recently attracted more attention as it involves no or less organic solvent [26]. The use of mechanochemical energy often results in oxygen-containing groups on the GNP surface.

Based on these literature studies, we have found the following knowledge gaps for polyurea nanocomposites: (i) design and preparation of polyurea matrices with tunable reaction rates, (ii) preparation of GNPs by environmentally friendly means, (iii) formation of a stable, strong interface between GNPs and polyurea through modification and (iv) addressing lack of multifunctionality, i.e. self-healing, electrical conductivity, thermal conductivity, corrosion resistance, impact resistance, etc. In this work, GNPs are exfoliated by mechanochemical treatment and then modified by isocyanate to create *IP*-GNPs for polyurea nanocomposites. Experiments are carried out to investigate the multifunctionality of the nanocomposites.

2. Experimental section

2.1. Materials

The graphite intercalation compound (GIC) was kindly provided by Asbury Carbons, Asbury, NJ, USA. Anhydrous ethanol and dimethylformamide (DMF) were purchased from Shanghai Sinopharm Chemical Reagent Company. Isophorone diisocyanate (IPDI) and polyaspartic acid ester (Desmophen NH 1420) were purchased from Costron, Germany. A long-chain diamine with a molecular weight of ~2000 (JEFFAMINE D-2000) and a long-chain triamine with a molecular weight of ~5000 (JEFFAMINE T-5000) were purchased from Huntsman, USA. All of the above materials and solvents were used directly without further purification.

2.2. Preparation of graphene nanoplatelets by mechanochemical treatment and their surface modification

Fig. S1a in the Supporting Information shows a schematic for preparation of graphene nanoplatelets (GNPs) by the mechanochemical treatment. A specific process is as follows: take 1 g of GIC and pour it into a crucible preheated at 700 °C in a muffle furnace, followed by 1-min heat treatment, to obtain worm-like expanded graphite. Then 1 g of the expanded graphite was transferred into a zirconia jar, into which 50 ml of ethanol, 10 g of zirconia balls of 6 mm in diameter, and 50 g of balls of 3 mm in diameter were added. The jar (cylindrical structure: 5 cm in diameter and 5 cm in height) was sealed and purged with nitrogen, followed by ball milling of 500 rpm for 12 h, resulting in a GNP suspension. The suspension was transferred to a beaker and sonicated in a water bath for 2 h under 20 °C. Finally, the GNP suspension was dried to obtain ball-milled GNPs.

In the next step, GNPs were modified with IPDI, and the preparation schematic and reaction scheme are shown in Fig. S1b and S1c of the Supporting Information, respectively. 0.1 g of ball-milled GNPs were placed into an agate mortar with 50 ml of DMF, followed by grinding for 10 min. The obtained mixture was transferred to a beaker and sonicated for 20 min under 20 °C to obtain a homogeneously dispersed GNP suspension. The GNP suspension was transferred to a three-neck flask, into which 2 ml IPDI was added; the reaction was carried out with magnetic stirring in an oil bath at 80 °C for 24 h. The mixture was filtered and repeatedly washed at least three times with DMF to remove excessive IPDI, and the product obtained after filtering was dried in an oven at 60 °C to obtain IPDI-modified GNPs (*IP*-GNPs).

In Fig. S1c of the Supporting Information, each IPDI molecule contains two isocyanate groups and these two groups have different activity. Because the quantity of isocyanate groups is obviously excessive in comparison with the surface groups of GNPs, most of the more active isocyanate groups would interact with the hydroxyl and carboxyl groups on the surface of GNPs, respectively generating carbamate bonds and amide bonds. As a result, the surface of IPDI-GNPs should still retain active isocyanate groups for the subsequent reactions with amino components in the polyurea system, to establish a robust bridge between GNPs and the matrix.

2.3. Preparation of polyaspartic polyurea/graphene nanocomposites

Fig. 1a–c illustrates the preparation of *IP*-GNP suspension, polyaspartic polyurea prepolymer/*IP*-GNP, and polyaspartic polyurea/*IP*-GNP nanocomposites, respectively. A typical preparation process is as follows. 0.1 g of *IP*-GNPs was charged into an agate mortar with 1 mL of DMF as the solvent, followed by grinding of 5 min. The mixture was transferred into a beaker and treated by an ultrasonication bath for 20 min at below 20 °C to obtain a homogeneously dispersed *IP*-GNP suspension.

As shown in Fig. 1b, 8 g of D2000 and 1.1 g of T5000 were transferred to a three-neck flask and mixed thoroughly, which was

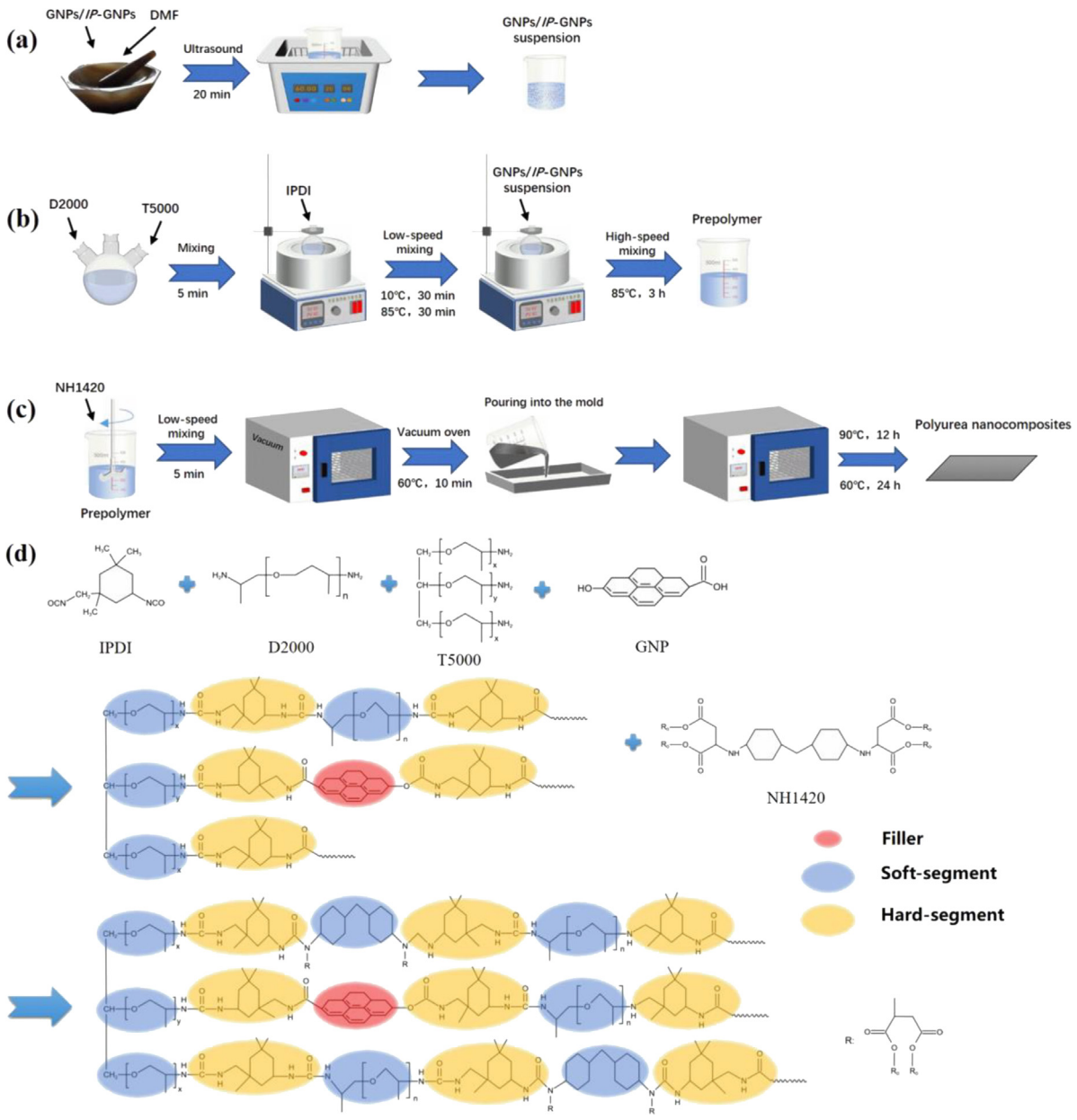

Fig. 1. Illustration for preparation of (a) *IP*-GNPs suspension, (b) polyaspartic polyurea/*IP*-GNP prepolymer, and (c) polyaspartic polyurea/*IP*-GNP nanocomposites, and (d) synthesis of polyaspartic polyurea/*IP*-GNP nanocomposites.

then placed in a thermostatic magnetic stirring oil bath, where the temperature was controlled at ~10 °C by using a liquid nitrogen cooling system. Subsequently, 4.1 g of IPDI was added slowly drop by drop with a low speed of stirring (30 rpm) for 30 min; when the temperature was raised to 85 °C, the reaction proceeded for another 30 min. After the stirring rate was increased to 120 rpm, the pre-prepared *IP*-GNP suspension was slowly added to the flask, followed by reaction of 3 h to obtain polyaspartic polyurea prepolymer/*IP*-GNP.

In Fig. 1c, 7.5 g of NH1420 was added to polyaspartic polyurea prepolymer/*IP*-GNP and stirred at low speed of 30 rpm for 5 min, followed by degassing in a vacuum oven at 60 °C for 10 min. The mixture was then poured into a PTFE mold and heated in an oven at 90 °C for 12 h to evaporate the remaining solvent. Finally, the material was cured in an oven at 60 °C for 24 h to obtain polyaspartic polyurea/*IP*-GNP nanocomposites. Fig. 1d shows the reaction scheme of polyaspartic polyurea/*IP*-GNP nanocomposites. The preparation of unmodified polyaspartic polyurea/GNP nanocomposites only requires replacing the *IP*-GNP suspension with a GNP suspension in the above process.

2.4. Characterization

Atomic Force Microscopy (AFM) was employed to investigate the surface morphology and the thickness of expanded graphite sheets, ball-milled graphene nanoplatelets (GNPs), ball-milled and ultrasonicated GNPs, and *IP*-GNPs, by using an AutoProbe CP/MT scanning probe microscope (Veeco Instruments) with a V-shaped "super-lever" probe B in a non-contact mode for imaging. All images were collected at a relative humidity of 50% and 23 °C with a scanning grating rate of 1 Hz.

The organic groups on the surface of ball-milled GNPs and *IP*-GNPs were analyzed by a Fourier Transform Infrared Spectrometer (FT-IR), a Bruker TENSOR II, by using a KBr method for sample preparation. Other testing parameters include a wave number range

of 500–4000 cm^{-1}, a characteristic incidence angle of 450°, and a resolution of 4 cm^{-1}.

The grafting ratio of *IP*-GNPs was studied using a TGA instrument under an inert (nitrogen) atmosphere. For thermogravimetric analysis, 5 mg of GNPs/*IP*-GNPs powders was placed in a 40 μl aluminum tray and sealed with a lid. The samples were heated from 28 to 640 °C at 10 °C min^{-1} while maintaining a constant nitrogen flow rate of 50 mL min^{-1}.

Transmission electron microscopy (TEM) was used to investigate the exfoliation and dispersion of GNPs and *IP*-GNPs in polyurea. The nanocomposites were cryo-microtomed to produce sections of 50–70 nm in thickness using a diamond knife. These sections were transferred to copper grids for TEM observation.

Scanning electron microscopy (SEM) was used to study the morphology of polyaspartic polyurea/*IP*-GNP nanocomposites. The tensile-fractured samples were glued onto a conductive substrate with conductive adhesive and then sprayed with gold at 10 mA for 45 s using an Oxford Quorum SC7620 sputter coater. Each sample was observed using a ZEISS Sigma 300 scanning electron microscope with an accelerating voltage of 3 kV.

The tensile properties and tear strength of polyaspartic polyurea nanocomposites were measured by a universal testing machine according to ISO 37-2005 and ISO 34-1:2004. The tensile specimens were 75 mm long, 4 mm wide, and 2.5 mm thick, with a gauge length of 25 mm. The pant-tear specimens were 150 mm long and 50 mm wide, with a pre-crack of 75 mm in length. For each component, at least five identical samples were tested and the average values were derived.

A Charpy impact tester was used to test the impact resistance. The samples were prepared according to ISO 179-1 and coated with 2 mm of polyaspartic polyurea or its nanocomposites. A pendulum with an impact energy of 15 J was selected, and the initial impact test speed was 3.8 m/s. Prior to testing, the machine was calibrated for energy dissipation due to air resistance and bearing friction.

The conductivity of polyaspartic polyurea/*IP*-GNP nanocomposites was measured at room temperature using an Agilent 4339B high resistivity meter equipped with a 16008B resistivity cell (two-point probe). Measurements were performed on samples with a thickness of 6.8 mm and a diameter of 24 mm according to ASTM D257-99. The data shown is the average of at least three measurements.

The thermal conductivity of polyaspartic polyurea and its nanocomposites was measured using a Hot Disk TPS 2500S instrument. Its testing principle is based on the transient planar heat source method, which allows the direct measurement of thermal conductivity in a range of 0.005–500 W/m K at −40 to 600 °C.

The swelling of a polymer is the phenomenon of mass increase due to the penetration of corrosive medium into the interior of the polymer. Being immersed in acid/alkali/salt solutions, polyurea and its nanocomposites were weighed every 2 days. The data were processed by Eq. (1):

$$w_1 = \frac{m_2 - m_1}{m_1} \times 100\% \quad (1)$$

Where w_1 is the polyurea dissolution rate, m_1 is the mass of polyurea before immersion, and m_2 is the mass after immersion for N days.

Corrosion of a polymer in a medium refers to a phenomenon where a fraction of macromolecules migrates by diffusion out to the medium, reducing the polymer mass. Being immersed in acid/alkali/salt solutions, polyurea and its nanocomposites were weighed every 2 days. To ensure a sample was dry and clean, each sample was carefully wiped and placed in an oven at 65 °C for 3 h before weighing. We processed the data by Eq. (2):

$$w_2 = \frac{m_3}{m_1} \times 100\% \quad (2)$$

where w_2 is the corrosion rate of the polyurea, m_1 is the mass of the polyurea before immersion, and m_3 is the mass of the polyurea after immersion for N days.

3. Results and discussion

3.1. Mechanochemically exfoliated graphene nanoplatelets and surface modification

As a green and efficient method, the mechanochemical treatment was used herein to prepare graphene nanoplatelets (GNPs) whose thickness was examined by atomic force microscopy (AFM). Fig. 2a shows a typical expanded graphite sheet, and the thickness was measured to be 119.2 ± 1.3 nm by examining 10 sheets. After 12 h of ball milling, the average thickness was reduced to 4.6 ± 0.3 nm in Fig. 2b. The mechanochemical energy generated during planetary ball milling is mainly contributed by shearing and impact force. The shearing force can effectively overcome the intermolecular van der Waals bonds and open the gap between the nanoplatelets, thereby reducing the thickness of GNPs [27]. At the same time, GNPs are crushed under the action of the impact force, leading to the reduction of the lateral dimensions [28].

Fig. 2c displays an AFM micrograph of GNPs obtained by combination of ball milling and ultrasonic treatment. Due to the ultrasonic cavitation effect [29–31], the GNP interlayer distance is further expanded and the layers are exfoliated, giving rise to lower average thickness, e.g. 3.4 ± 0.2 nm. Fig. 2d shows an AFM image of *IP*-GNPs modified by isocyanate (IPDI); the average thickness was measured to be 4.2 ± 0.1 nm, which is slightly thicker than the unmodified GNPs.

In order to further verify the existence of isocyanate functional groups on the surface of GNPs, we performed FT-IR tests before and after the modification. In Fig. 2e, GNPs reveal distinct characteristic absorption peaks at 3446 and 1382 cm^{-1}, indicating that the GNP surface contains a large amount of –OH groups [32,33]. The peak at 1729 cm^{-1} is attributed to the stretching vibration peak of the C=O group [24,33,34], indicating the existence of carboxyl groups on the surface. The absorption peaks at 1601 cm^{-1} and 1043 cm^{-1} correspond to the stretching vibrations of –OH (H_2O) and –C–O–C– groups [24,32], respectively. These characteristic peaks confirm the presence of a large number of oxygen-containing groups on the GNP surface which were introduced through the high-energy ball milling. During the process of planetary ball milling, shear strain energy accumulated within the GNP structures. When the accumulated energy reached a limit, the GNP edge would form partial local disintegration to absorb and release energy. Evidence shows that during milling the local temperature can reach ~1500 K [35]. Under the joint action of a local high temperature and strong mechanical force, the anhydrous ethanol in the ball-milling jar would rearrange the chemical bond network in the carbon skeleton, thereby generating hydroxyl, carboxyl, and other oxygen-containing functional groups on the surface of GNPs. These groups provide binding sites for the subsequent modification by IPDI.

In the FT-IR spectrum of *IP*-GNPs, the absorption peak at 1672 cm^{-1} corresponds to the C=O stretching in the CONH group. In comparison with those unmodified GNPs, the absorption peaks at 3446 cm^{-1} and 1382 cm^{-1} are significantly wider and stronger, corresponding to the NH stretching and bending (in-plane) and C–N stretching in the CONH group, respectively, indicating the formation of amide groups [24,33,36]. We observed the disappearance of the stretching vibration peaks of the carboxyl group at 1729 cm^{-1} and the oxygen-containing group at 1043 cm^{-1} in GNPs as well as the appearance of the stretching vibration peak of the methyl group at 2921 cm^{-1} in *IP*-GNPs, all of which indicate the generation of the carbamate group [36,37]. The appearance of a new absorption peak at 2363 cm^{-1} corresponds to the stretching vibration of the –NCO group [34,36,37], inferring the successful grafting of the isocyanate groups on GNPs. This is due to the large difference in activity of the two –NCO bonds in IPDI. The one with higher activity reacts with the hydroxyl and carboxyl groups on the surface of GNPs to form carbamate and amide bonds, while the other –NCO bond is retained due to its lower activity, providing conditions for the subsequent reaction of *IP*-GNPs with the polyetheramine in polyurea, as supported by a previous work [38].

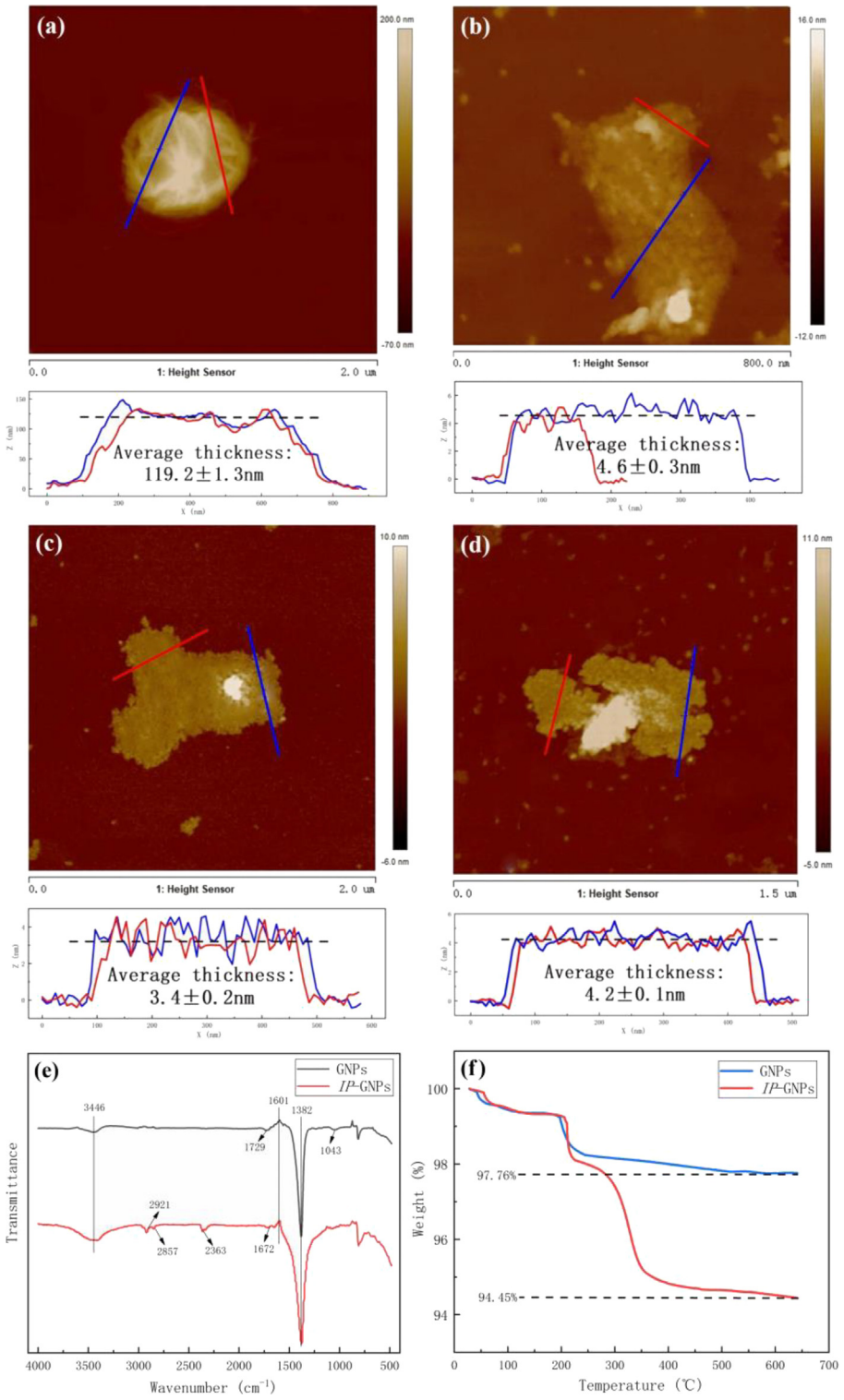

Fig. 2. AFM images and corresponding height profiles of (a) expanded graphite, (b) ball-milled GNPs, (c) GNPs exfoliated by ball milling and sonication treatment, and (d) *IP*-GNPs; (e) FT-IR spectra and (f) TGA curves of GNPs and *IP*-GNPs.

The amount of IPDI grafted onto GNPs was investigated by thermogravimetric analysis. In Fig. 2f, two similar weight loss peaks are seen for GNPs and *IP*-GNPs. The first weight loss phase is from 40 to 80 °C, corresponding to the loss of free water from GNPs and *IP*-GNPs. The second weight loss phase occurs from 200 to 230 °C, due to the pyrolysis of oxygen-containing groups present in GNPs and *IP*-GNPs. In comparison with GNPs, *IP*-GNPs exhibit one more obvious weight loss peak at 280–360 °C, which corresponds to the pyrolytic shedding of IPDI grafted on the surface of *IP*-GNPs. At 640 °C, the residue weight percentages of GNPs and *IP*-GNPs are 97.76% and 94.45%, respectively, with a 3.31% difference.

3.2. Variables for the synthesis of polyaspartic polyurea

As the typical feature of polyurea, its hardness and softness can be readily manipulated in a proper range by adjusting the isocyanate index

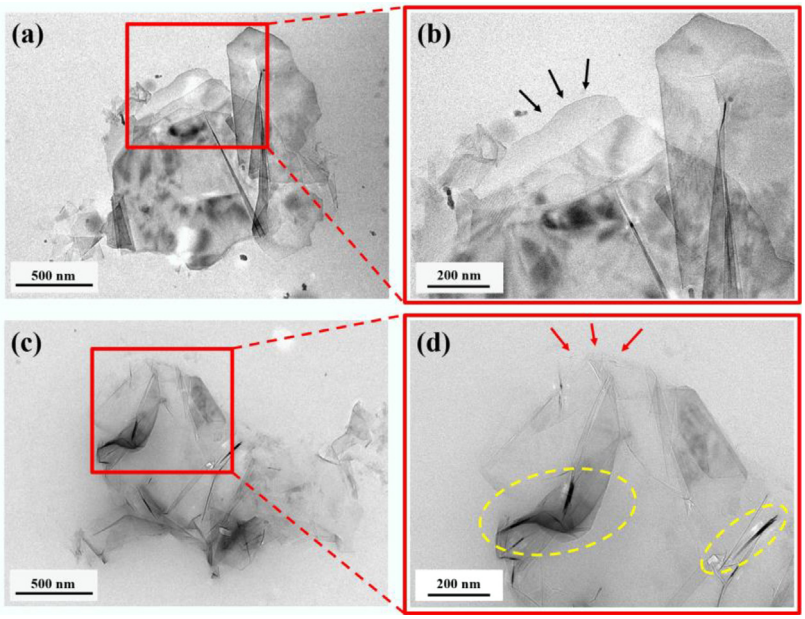

Fig. 3. TEM images: (a) and (b) for a polyaspartic polyurea/GNP nanocomposite and (c) and (d) for a polyaspartic polyurea/*IP*-GNP nanocomposite, both at 1.25 vol%.

and the free isocyanate content [39,40]. In this study, we attempted to obtain a polyaspartic polyurea elastomer with high tensile strength and excellent elongation at break. Detailed experimental procedures and discussions are given in Section 1 and Fig. S2 of the Supporting Information.

3.3. Morphology of polyaspartic polyurea/graphene nanocomposites

The filler dispersion in the matrix and the interfacial effect pose a significant effect on the performance of nanocomposites [20]. TEM was used to investigate the dispersion of GNPs and *IP*-GNPs in the polyaspartic polyurea matrix as well as the interfacial effect [32,41]. Since thin GNPs possess light transmission of up to 97.73% [28], it is a challenge to use TEM to characterize the morphology at low filler fractions (less than 0.25 vol%). It is a daunting challenge to make sections of a nanocomposite which contains high fractions of GNPs, due to the striking contrast in modulus between GNPs and polyurea. Therefore, we have selected the 1.25 vol% sample.

In Fig. 3a, we found serious stacking of GNPs in polyurea, indicating that unmodified GNPs cannot readily exfoliate and disperse in the matrix due to the strong interlayer van der Waals interactions. At a higher magnification in Fig. 3b, a clear interface between GNPs and polyurea is observed as shown by black arrows. By contrast, we can see an obviously lower degree of stacking of *IP*-GNPs in Fig. 3c. Red arrows pointed bout blurred interface area between *IP*-GNPs and polyurea at a higher magnification in Fig. 3d. The improved exfoliation and interface are attributed to the presence of isocyanate groups on the surface of *IP*-GNPs. As discussed in Section 3.1, these groups provide GNPs opportunities to participate in the polyurea synthesis, by bridging *IP*-GNPs with polyurea macromolecules through chemical bonding. This will likely result in not only improvement of the mechanical properties but new functionalities as to be reported later in this work. The dark-color structures (as marked by the yellow dashed circles) in Fig. 3d are actually folded graphene [32].

3.4. Mechanical properties

In Fig. 4a, tensile strength increases with GNPs and reaches a maximum of 12.41 ± 0.22 MPa at 0.05 vol%. At higher fractions, tensile strength decreases likely because GNPs were locally agglomerated in polyurea resulting in stress concentration sites under loading. Although polyaspartic polyurea/*IP*-GNP nanocomposites display a similar trend at 0.05 vol%, the maximum tensile strength of 15.72 ± 0.67 MPa is 26.67% higher than the unmodified system.

In Fig. 4b, the elongation at break for polyaspartic polyurea/GNP nanocomposites is found to decrease with GNPs, probably due to the inert surface of GNPs [20]. As discussed in Fig. 3, GNPs form a sharp interface with polyurea and thus they would cause a spacer effect, similar to many physical inserts in the matrix, reducing the elongation at break. In comparison, the elongation at break of polyaspartic polyurea/*IP*-GNP nanocomposites increases with *IP*-GNPs until till 0.05 vol% and then decreases. The maximum elongation at break 463.58 ± 9.33% is seen at 0.05 vol% of *IP*-GNPs. The reason is attributed to a fact that the isocyanate groups of *IP*-GNPs can produce chemical bonding with the polyurea matrix, which in turn would distribute the stress more uniformly throughout the polyurea matrix and transfer stress more efficiently across the interface. Fig. 4c demonstrates the same pattern as that in Fig. 4a, where the tear strength of polyaspartic polyurea/GNP nanocomposites increases with GNPs; a maximum tear strength 43.19 ± 1.31 kN/m is seen at 0.05 vol%. Similarly, a polyaspartic polyurea/*IP*-GNP nanocomposite at 0.05 vol% has the maximum tear strength of 46.71 ± 0.66 kN/m, representing an increment of 8.15% over the unmodified nanocomposite.

To further investigate the dispersion of GNPs and the improvement of the interface on the morphological properties of polyaspartic polyurea nanocomposites, we investigated their tensile-fractured surface by SEM. In the Supporting Information Fig. S3 for pure polyaspartic polyurea, the fracture surface has no obvious features at low magnifications. At a high magnification, many microcracks are found to extend randomly. By contrast, less cracks and a lower degree of rupture are seen on the fracture surface of the polyaspartic polyurea/*IP*-GNP nanocomposite at 0.05 vol% in Fig. 4d. This indicates that the incorporation of the modified GNPs into the polyurea matrix has reduced the crack generation through the crack deflection mechanism [42], resulting in smoother fractured surfaces. In Fig. 4e, *IP*-GNPs appear to be well embedded in the polyurea matrix as no obvious filler particles can be seen except the one in the middle. This is because the isocyanate groups grafted on GNPs would bond with the terminal amine groups of polyether to form urea bonds as shown in Fig. 1d, intimately integrating GNPs with the matrix. An enlarged image in Fig. 4f clearly shows that the surface of *IP*-GNPs contains a large number of folds and fracture occurs at the tips of the folds (marked by the red dashed circles). It

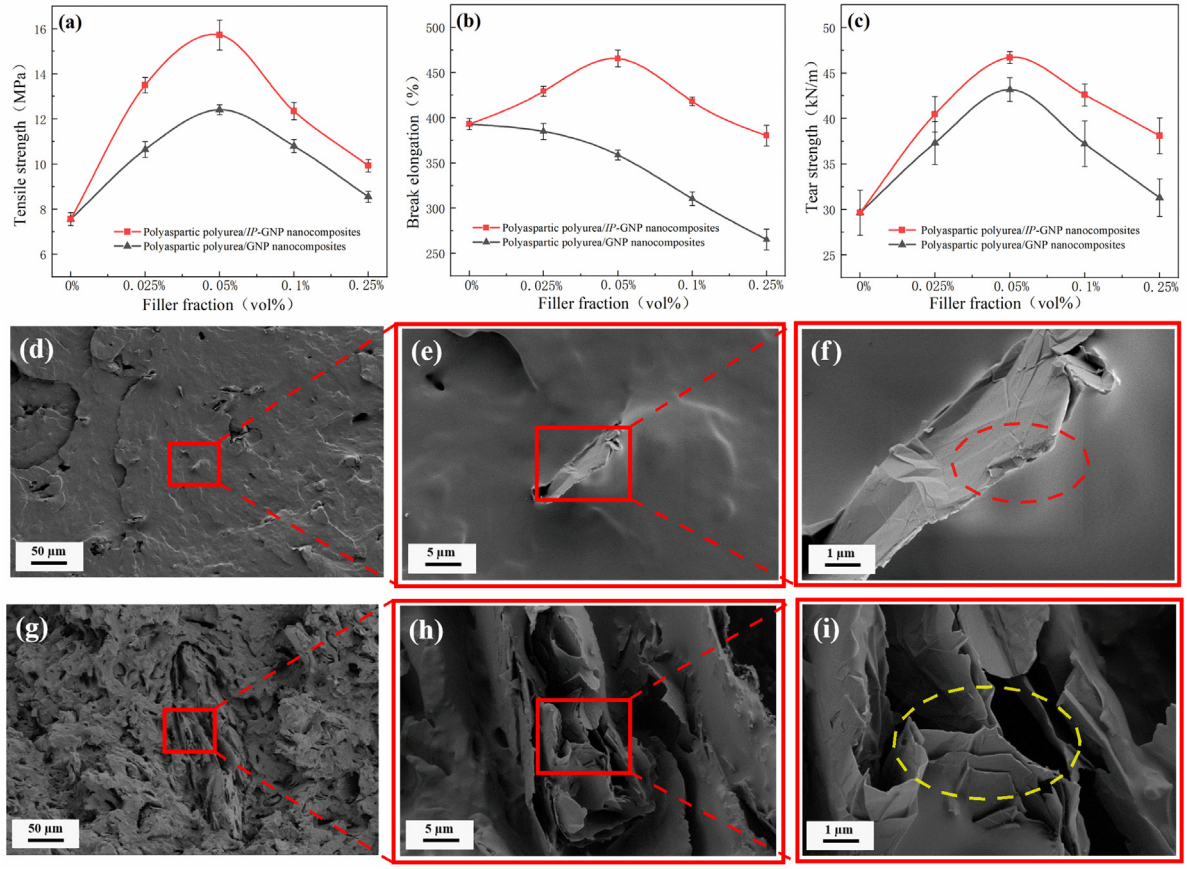

Fig. 4. Mechanical properties of nanocomposites: (a) tensile strength, (b) elongation at break, and (c) tear strength; SEM images of tensile-fractured nanocomposites with *IP*-GNPs: (d), (e), and (f) at 0.05 vol% and (g), (h), and (i) at 0.25 vol%.

implies effective load transfer from the matrix to *IP*-GNPs, enhancing the mechanical properties [43].

Fig. 4g shows the tensile-fractured surface of a polyaspartic polyurea/*IP*-GNP nanocomposite at 0.25 vol%. The surface is rough and uneven in comparison with Fig. 4d. This indicates that adding higher fractions of *IP*-GNPs has caused agglomeration, which would not only weaken the stress transfer from the matrix to the sheets but cause stress concentration. A large amount of agglomeration can be seen in Fig. 4h and i (as marked by the yellow dashed circles), which leads to micro-pores and gaps around the agglomeration site. This results in the weakened of the interface bonding strength between the *IP*-GNPs and the polyurea matrix. Under loading, fracture always initiates from these defects. This explains the reduction of the mechanical properties at higher fractions.

3.5. Self-healing properties

An intrinsically self-healing material relies on its own internal dynamic covalent or non-covalent bonding to generate a healing drive upon external stimuli such as light and heat, to repair spontaneously the damaged or fractured parts [44–46]. The theoretical foundation of self-healing in this study is the large number of reversible dynamic hydrogen bonds in the polyaspartic polyurea molecular chain as per the discussion in Fig. 1d [47]. We selected pure polyurea and its nanocomposites containing either GNPs or *IP*-GNPs at 0.05 vol% to investigate the healing efficacy.

Three groups of dumbbell-shaped tensile specimens refer to samples made of pure polyurea, polyaspartic polyurea/GNP nanocomposite and polyaspartic polyurea/*IP*-GNP nanocomposites, respectively. In a typical experiment, a specimen was incised along the midline by a scalpel at 45°, to produce two separate pieces. The pieces were then aligned along the midline and heated in an oven at 60 °C for certain time. In the enlarged images in Fig. 5a, the pieces were joined afterwards. To prove that the polyaspartic polyurea nanocomposites prepared in this work have excellent self-healing properties, we joined a half piece of pure polyurea specimen with a half piece of the modified nanocomposite specimen, to create a hybrid specimen. All healed specimens were tested with mechanical loading of a 4 LB dumbbell plate. In Fig. 5b, the plate is readily lifted by the hybrid specimen, highlighting the superior self-healing functionality of the nanocomposites.

Inspired by the Wool and O'Connor's healing model [48], we developed a self-healing mechanism model for our nanocomposites, as shown in Fig. 5c. The microscopic self-healing process of polyurea nanocomposites is described in three phases. In the first phase, the polymer chains near the cross-section disentangle and diffuse into the cut-off region under the stimulation of thermal energy. In the second phase, the molecular chains at both specimen ends can further diffuse beneath the interface, resulting in a strong interface. The motion of soft segments can drive the motion of hard segments, creating a healing force within the material matrix (as indicated by yellow arrows in Fig. 5(c). In the third phase, when the cleaved hard segment domains inter-diffuse and meet under the healing force, they form new intact hard segments facilitated by the dynamic interactions of internal hydrogen bonds. With the deepening of the random interaction, the soft and hard chain segments are re-entangled, enabling the nanocomposite to accomplish self-healing.

To evaluate the healing efficiency of polyaspartic polyurea and its nanocomposites, we tested tensile strength and elongation at break of pristine polyurea/nanocomposite and the repaired polyurea/ nanocomposite, respectively. R_T and R_B in Eqs. (3) and (4) represent the tensile strength healing efficiency and elongation at break healing efficiency of

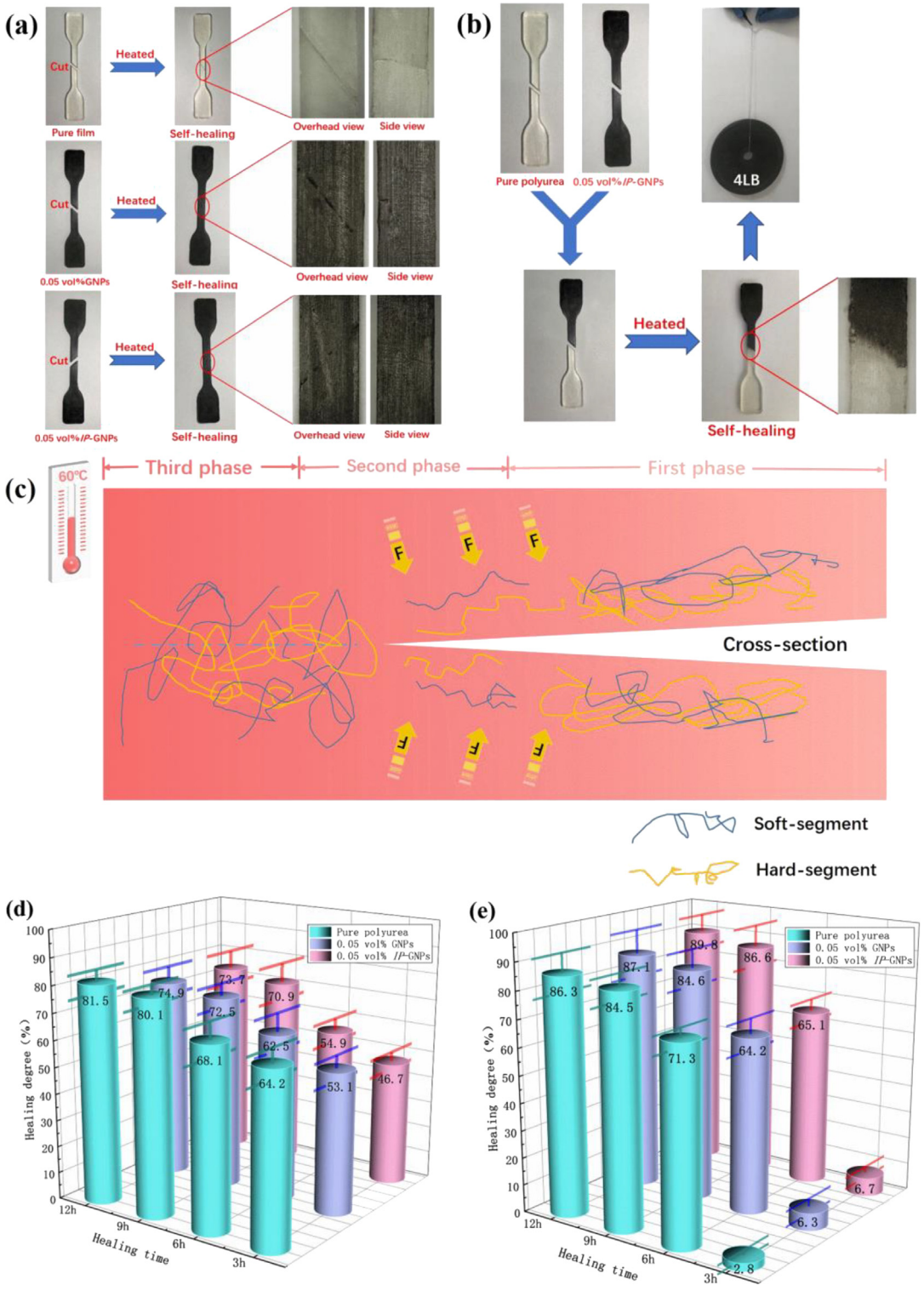

Fig. 5. (a) Healing effect graph of polyaspartic polyurea and its nanocomposites, (b) image of self-healed tensile samples subjected to 4LB weight dumbbell, (c) model graph of polyurea self-healing mechanism, (d) tensile strength healing efficiency graph, and (e) elongation at break healing efficiency of polyaspartic polyurea and its nanocomposites.

polyurea and its nanocomposites, respectively.

$$R_T = \frac{\sigma_0}{\sigma_b} \times 100\% \tag{3}$$

$$R_B = \frac{\varepsilon_0}{\varepsilon_b} \times 100\% \tag{4}$$

Where σ_b and ε_b are the tensile strength and elongation at break of polyurea and its nanocomposite before cutting, and σ_0 and ε_0 are tensile strength and elongation at break of the polyurea and its nanocomposites after cutting and healing. We have found that the healing efficiency of the three groups increases with the heating time.

Since a high healing temperature might pose a negative effect on the cost and thermal stability [49], we have selected 60 °C as the repair temperature. Fig. 5d and e reveals the healing efficiency graphs with heating time. With a short healing time of 3 h, R_T of the polyurea and nanocomposites can reach ~50% but R_B is ~5% only. However, when

the heating time reaches 9 h, the healing efficiency seems to reach a peak (~72% for R_T and ~85% for R_B). After heating for 12 h, R_T and R_B only increase to ~75% and ~87%, respectively. This is because that the dynamic interaction between hydrogen bonds and the randomized cross-diffusion of chain segments needs time to reach saturation. In view of energy consumption and production efficiency, 9 h is an ideal healing time.

In order to investigate the effect of graphene surface modification on the self-healing properties of polyurea, we employed the same heating time 9 h to compare the healing efficiency between pure polyurea and its nanocomposites at 0.05 vol% in terms of tensile strength. In Fig. 5d, the tensile strength of the unmodified nanocomposite is 7.6% lower than polyurea, because the presence of graphene nanoplatelets (GNPs) likely hinders the random interaction and crosslinking of molecular segments. The polyurea/*IP*-GNP nanocomposite exhibits a tensile strength healing efficiency being 9.2% lower than polyurea. This is likely because the covalent bonds between the *IP*-GNPs and the polyurea molecular chains are broken, and they cannot be reconstituted by thermal stimulation alone.

In Fig. 5e, the elongation at break healing efficiencies of the nanocomposites have been further improved by 0.1% and 2.1% over polyurea. This is largely due to a fact that during the self-healing process, the nanoplatelets as physical barriers would affect the reconstruction of hydrogen bonds between the hard segments of the molecular chain, which reduces the crosslinking density of polyurea, as supported by previous studies [50,51]. The interface modification promoted the exfoliation and dispersion of the nanoplatelets. This means more platelets and their better dispersion in the modified nanocomposite, which would more effectively reduce the crosslinking density of polyurea.

And we observed that the mechanical properties of all three groups of polyurea after healing could not reach the level before cutting. This is likely due to the entanglement of molecular chains and the formation of a network of new hard chain segments that can impede the movement of molecular chains, causing a decrease in the mechanical properties of the healed polyurea [52]. Therefore, polyurea and its nanocomposites showed a small decrease in mechanical properties after healing.

Furthermore, we explored the multiple cutting-healing properties of polyaspartic polyurea and its nanocomposites, the results of which are shown in the Supporting Information Section 2.

In addition to the above excellent mechanical and self-healing properties, the nanocomposites also have certain impact resistance properties as elaborated in the Supporting Information Section 3.

3.6. Electrical conductivity

Fig. 6 demonstrates electrical conductivity of polyaspartic polyurea nanocomposites. At 3.82 vol%, the conductivity shows an abrupt change of seven orders of magnitude, which indicates that a conductive network has been established by GNPs in the matrix. After the percolation threshold is reached, further addition of *IP*-GNPs or GNPs does not contribute significantly to the conductivity. At the highest fraction of *IP*-GNPs, 8.05 vol%, the electrical conductivity was measured as 8.19×10^{-2} S/cm. At the same filler fraction, polyaspartic polyurea/*IP*-GNP nanocomposites exhibit higher conductivity than the unmodified nanocomposites, due to the interfacial modification which resulted in more exfoliated and uniformly dispersed GNPs in the matrix. In order to determine the percolation threshold for the polyaspartic polyurea/*IP*-GNP (GNP) nanocomposites, we fitted the experimental data to the power law Eq. (5) for further analysis:

$$\sigma_c \propto (\varphi - \varphi_{th})^t \tag{5}$$

where σ_c is the nanocomposite conductivity, φ is the volume fraction of GNPs, φ_{th} is the permeation threshold expressed as a volume fraction, and t is a generic critical exponent that depends on the size of the formed network. By fitting the experimental data, we obtained φ_{th} = 3.61 vol% and t = 1.97 for the polyaspartic polyurea/*IP*-GNP nanocomposites. The value t is very close to the theoretical critical exponent value of 1.9 for the 3D conductive network [53]. This threshold value implies that a complete 3D conductive network is constructed inside the polyurea matrix at 3.61 vol% of *IP*-GNPs.

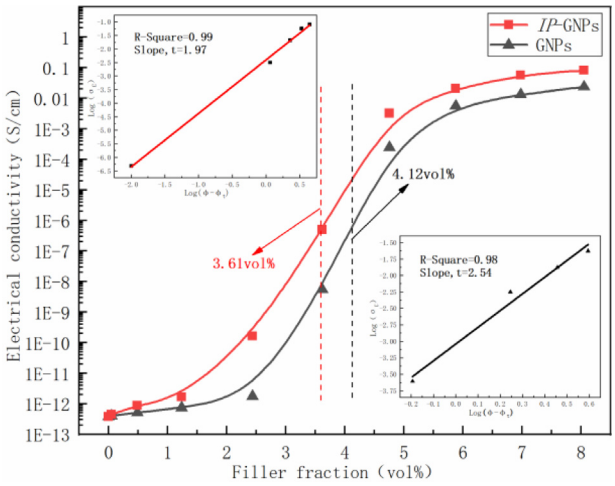

Fig. 6. Electrical conductivity of polyaspartic polyurea/GNP nanocomposites.

3.7. Thermal conductivity

Thermal conductivity consists of phonon (lattice) thermal conductivity and electronic thermal conductivity. For polymers, it often depends on the phonon thermal motion, and it is challenging to transfer phonon motion between polymer chains due to low crystallinity. Highly thermally conductive fillers, such as graphene, carbon nanotubes and hexagonal boron nitride, are often selected to enhance the thermal conductivity of polymers [54–56]. It is thus anticipated that the incorporation of GNPs in the polyaspartic polyurea should result in high thermal conductivity.

In Fig. 7a, pure polyaspartic polyurea has a thermal conductivity of merely 0.09 W/m K, and it increases obviously with GNPs and *IP*-GNPs. At a low fraction range (<4.76 vol%), the thermal conductivity increases incrementally. A significant upward trend can be seen at over 4.76 vol%. The nanocomposites containing 4.76 vol% of either unmodified or modified GNPs were found to have thermal conductivity of 1.25 and 1.67 W/m K, respectively, representing increments of 1,288.89% and 1,755.56% over pure polyurea. At 7.00 vol%, the thermal conductivity reaches 21.44 W/m K for polyaspartic polyurea/GNP nanocomposites and 38.49 W/m K for polyaspartic polyurea/*IP*-GNP nanocomposites, corresponding to increments of 23,722.22% and 42,666.67%, respectively.

Fig. 7b illustrates SEM micrographs of a polyaspartic polyurea/*IP*-GNP nanocomposite at 1.24 vol%. The samples were prepared by fracturing after freezing in liquid nitrogen; such a low temperature was used to ensure the matrix exerts no effect on the morphology of *IP*-GNPs during sample preparation. *IP*-GNPs dispersed in the matrix are found to have rare contact with each other, so the electron thermal overfiltration between *IP*-GNPs would remain low at this stage. Meanwhile, the interface between *IP*-GNPs and polyurea may produce a certain phonon scattering and thus reduce the thermal conductivity. Noted that the main carriers of heat conduction in the polymer and GNPs are phonons. Therefore, only incremental improvements of thermal conductivity were seen at below 4.76 vol%.

Fig. 7c contains SEM images of polyaspartic polyurea nanocomposites at 4.76 vol% of *IP*-GNPs. The distance between GNPs becomes smaller and certain GNPs contact each other, gradually forming a thermal conductivity pathway in the polyurea matrix. This macroscopically

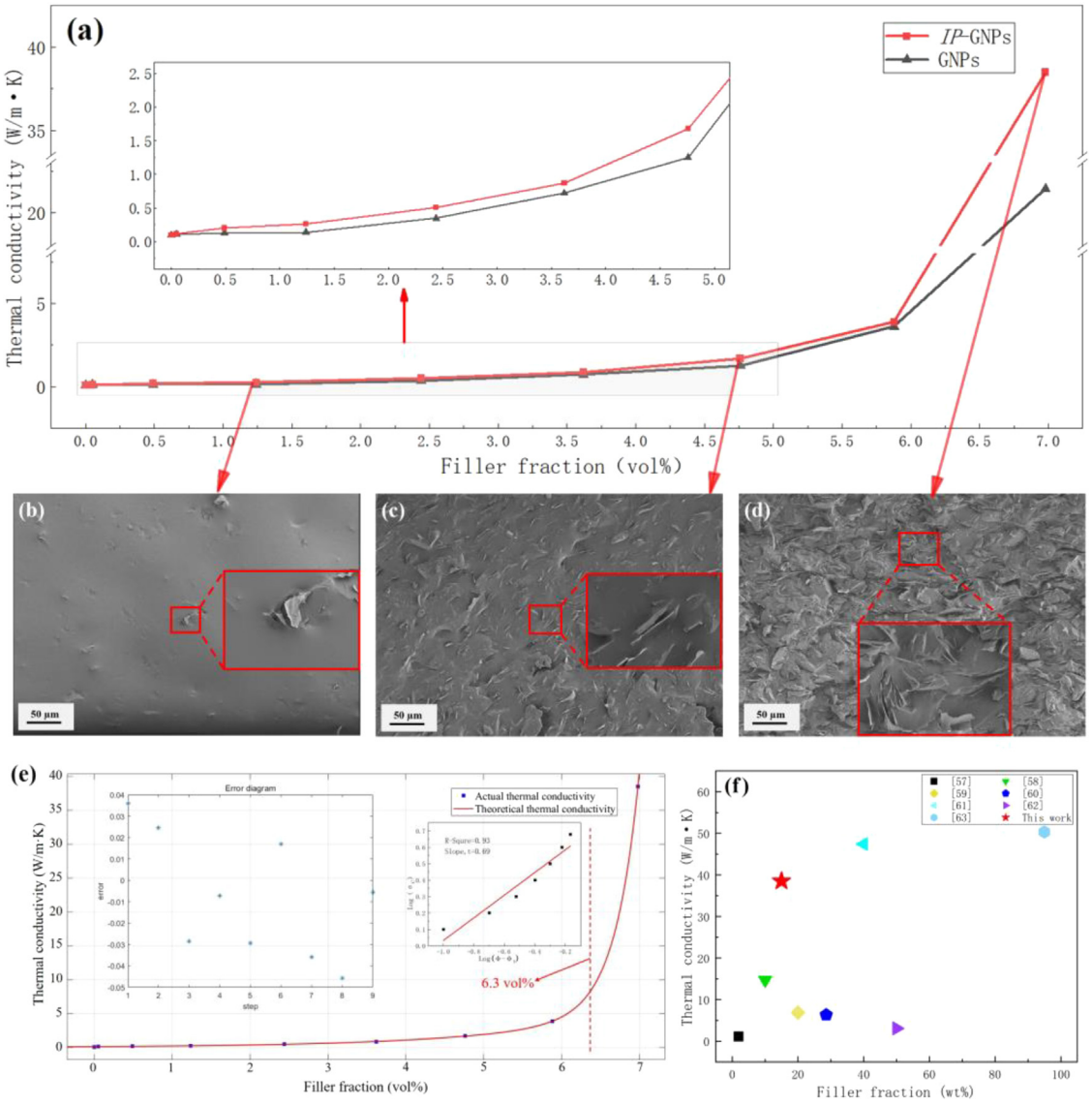

Fig. 7. Thermal conductivity of polyaspartic polyurea/graphene nanocomposites (a), SEM images of freeze-fractured surface of a polyaspartic polyurea/*IP*-GNP nanocomposite at 1.2 vol% for (b), at 4.7 vol% for (c), and at 7.0 vol% for (d), prediction of thermal conductivity of polyaspartic polyurea/*IP*-GNP nanocomposites (e), and comparison of our thermal conductivity with those reported (f).

implies that the thermal conductivity of the nanocomposites starts to rise significantly. Fig. 7d contains SEM images of polyaspartic polyurea nanocomposites at 7.00 vol% *IP*-GNPs. The distance between graphene nanoplatelets becomes narrow and more GNPs contact each other, resulting in drastic increments of electrical and thermal conductivities. At higher filler fractions, the electron thermal conductivity would play a dominant role for the nanocomposites whereas the adverse effect of phonon scattering at the interface between GNPs and the polyurea matrix would diminish.

In Fig. 7a, polyaspartic polyurea/*IP*-GNP nanocomposites have higher thermal conductivity than unmodified nanocomposite systems. This might be due to a fact that *IP*-GNPs due to surface modification can disperse more uniformly in the polyurea matrix forming a stronger interface; These robust interfaces can effectively promote electron transfer and heat energy transfer. Both the unmodified and modified nanocomposites demonstrate drastic improvements of thermal conductivity at high filler fractions, which is also known as the thermal permeability phenomenon. This phenomenon has been rarely reported for polymer nanocomposites in comparison with the electrically conductive percolation threshold [54,57]. In order to further investigate the thermal permeability phenomenon of polyaspartic polyurea/*IP*-GNP nanocomposites, we selected the thermal conductivity of the nanocomposites of different fractions of *IP*-GNPs, fitted a curve of thermal conductivity with the fractions (Fig. 7e), and used MATLAB to derive and obtained the following equation (Eq. (6)):

$$Thermal\ conductivity = 0.13e^{0.53x} + 3.79 \times 10^{-9} e^{3.28x} \quad (6)$$

Where x denotes the volume fraction of *IP*-GNPs in polyurea. The error analysis of the thermal conductivity data obtained by fitting the equation with the experimentally measured thermal conductivity data was performed using MATLAB, and the results of the calculation are shown in Fig. 7e. It can be found that the error bars are less than 0.05 W/m K, which means that the thermal conductivity equation model established in this work can be used to predict the thermal conductivity of polyurea nanocomposites at 0–7.00 vol% of *IP*-GNPs. Based on the thermal conductivity equation model (Eq. (6)), we deduced that the theoretical permeability threshold of polyaspartic polyurea/*IP*-GNP nanocomposites is 6.30 vol%. Similarly, we performed the same analysis for the unmodified polyaspartic polyurea/GNP nanocomposites, and the results are shown in the Supporting Information Section 4.

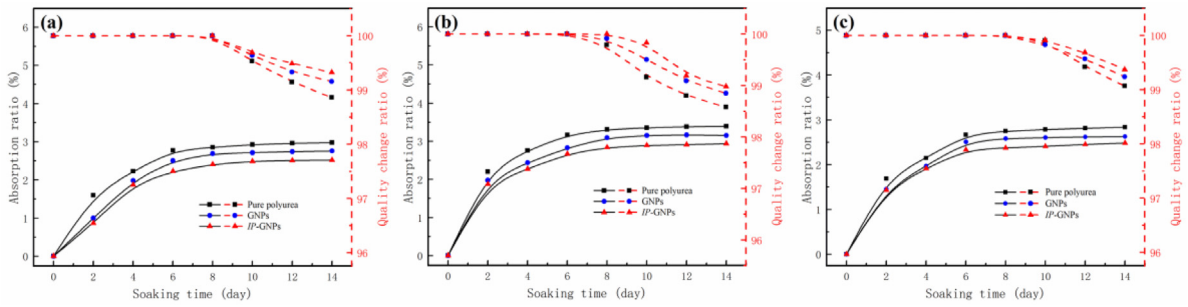

Fig. 8. Chemical resistance of polyaspartic polyurea and its nanocomposites in (a) H_2SO_4 solution, (b) NaOH, and (c) NaCl. (For interpretation of the references to colour in this Fig. legend, the reader is referred to the web version of this article.)

Fig. 7f reveals the thermal conductivity of our 7.00 vol% (15.00 wt%) nanocomposite in comparison with the data reported in the literature [57–63]. It is worth to mention that the nanocomposite was found to have a tensile strength of 0.32 MPa and a fracture strain of 340%. The low strength would be caused by the thermally conductive network formed by graphene. Hence, the fraction of graphene must be carefully selected in practice to reach a balance between desirable mechanical strength and thermal conductivity. The nanocomposite has higher conductivity than those literature values due to the following factors:

(i) High filler fractions, if uniformly dispersed or forming conducting network in the matrix, should promote the thermal conductivity of polymers. Nanofillers have varying thermal conductivities and there is always a large difference between the theoretical values and the actual measured ones, as indicated in Table 1 [54,64–70]. For example, the theoretical thermal conductivity of graphene can reach 5300 W/m K. However, the thermal conductivity of some GNPs and graphene oxides reported in the literature is only 100–800 W/m K [54]. The thermal conductivity of other typical 2D materials, such as boron nitride, is found to be ~200 W/m K, which is also much lower than its theoretical value in the literature [64]. These created a wide range of thermal conductivity of polymer nanocomposites prepared using different thermally conductive fillers [61,63,71] and it is a daunting challenge to achieve satisfactory conductivity at a low filler fraction.

(ii) Building a thermally conductive network can effectively enhance the thermal conductivity of polymeric materials [72]. Xiao et al. built a thermally conductive network with aromatic polyamide nanofibers containing 40–70 wt% oriented BN sheet crystals, leading to a thermal conductivity of 47.4–122.5 W/m K [61]. However, the process of building thermally conductive skeletons is often complicated and difficult to prepare in mass production, making it challenging for industrial applications.

(iii) Finally and the most importantly, a well-constructed filler-matrix interface is crucial for improving the thermal conductivity of polymer nanocomposites, as a good interface would not only promote the exfoliation of GNPs and create more uniformly dispersed nanoplatelets in the matrix but also effectively facilitate electron transport and thermal energy transfer in the matrix. In this study, the modification of GNPs with isocyanate has provided a strong interfacial interaction between *IP*-GNPs and the polyurea matrix, resulting in excellent thermal conductivity at a high filler fraction.

3.8. Chemical resistance

To investigate the chemical resistance of polyaspartic polyurea/graphene nanocomposites, we immersed certain specimens in solutions of acid (H_2SO_4, 5.00 wt%), base (NaOH, 5.00 wt%) or salt (NaCl, 5.00 wt%) for 14 days and measured their swelling and corrosion rates regularly. Since the nanocomposite at 0.05 vol% of GNPs showed the best mechanical properties, it was selected in this Section.

Table 1
Theoretical and those measured thermal conductivity of nanomaterials.

Nanofillers	Theoretical thermal conductivity (W/m K)	Actual measured thermal conductivity (W/m K)
Graphene	5300 [54]	~600 [65]
Boron nitride	2000 [66]	~300 [64]
CNTs	3500 [67]	~200 [68]
MXene	470 [69]	~100 [70]

We have processed the swelling test data, as detailed in Section 2.4. The color curves at the bottom in Fig. 8a–c indicate that the swelling (absorption) ratio of pure polyurea and its nanocomposites increases significantly during the first few days, whilst the weight gain tends to be level after Day 8. This may be due to the saturated absorption of acid/base/salt solution medium by polyurea and its nanocomposites. It is also evident that the addition of GNPs (*IP*-GNPs) improves the swelling resistance of polyurea. This is mainly owing to the existence of nanoplatelets in the polyurea matrix hindering the diffusion of acid/base/salt medium in polyurea.

The upper color curves in Fig. 8a–c represent the corrosion ratios (mass change rate). The mass does not change significantly within the first 6 days, indicating that the polyurea and its nanocomposites does not seriously corrode. After 6 days, the mass changes to varying degrees, indicating that they would have localized corrosion in the acid/alkali/salt solution for a long time and begin to dissolve in the acid/alkali/salt solution. Combining the dissolution and corrosion data of polyurea nanocomposites in acid/alkali/salt solutions, we can see that the corrosion resistance of polyaspartic polyurea/*IP*-GNP nanocomposites is better than the GNP system. This is because *IP*-GNPs have a strong interface with polyurea and the good dispersion, resulting in better corrosion resistance.

The results of tensile tests of polyaspartic polyurea and its nanocomposites after 14 days of corrosion are shown in Table S2 in the Supporting Information. Polyurea and its nanocomposites still maintain ideal mechanical properties in salt solution, but their properties decrease slightly in alkaline solution. The pure polyurea film in the alkali solution reveals the most obvious reduction in performance, i.e. reduction of tensile strength by 5.70% and the elongation at break by 3.90%. Hence, polyaspartic polyurea nanocomposites possess excellent chemical resistance and can be used as smart protective coatings.

Conclusion

(i) The mechanochemical treatment by ball milling not only reduced the thickness of graphene nanoplatelets (GNPs), but also introduced oxygen-containing functional groups such as hydroxyl groups and carboxyl groups. The surface of GNPs was covalently modified by isocyanate groups to establish a strong interface with the polyurea matrix.

(ii) Modulating the isocyanate index (1.05) and free isocyanate content (9.00%) resulted in desirable tensile strength and elongation at break for polyaspartic polyurea. The addition of *IP*-GNPs to polyurea significantly improved the mechanical properties.
(iii) The self-healing performance of polyaspartic polyurea was demonstrated for the first time. Our nanocomposites exhibited excellent resistance to acid, alkali and salt erosion.
(iv) The electrical percolation threshold of polyaspartic polyurea/*IP*-GNP nanocomposites was observed at 3.61 vol%, and the thermal conductivity reached 38.49 W/m K at 7.00 vol% of *IP*-GNPs.

CRediT authorship contribution statement

Qingshi Meng: Writing – original draft, Project administration. **Peng Wang:** Writing – review & editing, Writing – original draft, Methodology. **Yin Yu:** Writing – review & editing. **Jianbang Liu:** Investigation. **Xiao Su:** Investigation. **Hsu-Chiang Kuan:** Writing – review & editing. **Baozhu Wang:** Resources. **Liqun Zhang:** Writing – review & editing, Formal analysis. **Yingyan Zhang:** Resources, Methodology. **Dusan Losic:** Writing – review & editing, Methodology. **Jun Ma:** Writing – review & editing, Resources.

Declaration of competing interest

The authors claim no conflict of interest in this work.

Data availability

Data will be made available on request.

Acknowledgments

The National Natural Science Foundation of China (52173077& 51973123), the Liaoning Provincial Department of Education Series Project, Australia (LJKZ0187), the Natural Science Foundation of Liaoning Province (2023-MS-239), and the Liaoning BaiQianWan Talents Program, Australia (2021921081). JM thanks Australian Research Council, Australia (DP220103275) for financial support. The authors would like to thank Mr Guoji Guo for his solid preliminary work in this project. DL/JM support from the ARC Research Hub for Graphene Enabled Industry Transformation, Australia (IH15000003).

Appendix A. Supplementary data

Supplementary material related to this article can be found online at https://doi.org/10.1016/j.tws.2023.110853.

References

[1] L. Zhang, C. Ji, X. Wang, Y. Wang, G. Wu, H. Zhu, Z. Han, Strengthening and converse strengthening effects of polyurea layer on polyurea–steel composite structure subjected to combined actions of blast and fragments, Thin-Walled Struct. 178 (2022) 109527.
[2] W. Wang, W. Lu, A. Goodwin, H. Wang, P. Yin, N.-G. Kang, K. Hong, J.W. Mays, Recent advances in thermoplastic elastomers from living polymerizations: Macromolecular architectures and supramolecular chemistry, Prog. Polym. Sci. 95 (2019) 1–31.
[3] E. Yildirim, M. Yurtsever, The role of diisocyanate and soft segment on the intersegmental interactions in urethane and urea based segmented copolymers: A DFT study, Comput. Theoret. Chem. 1035 (2014) 28–38.
[4] E. Badamshina, Y. Estrin, M. Gafurova, Nanocomposites based on polyurethanes and carbon nanoparticles: preparation, properties and application, J. Mater. Chem. A 1 (22) (2013) 6509–6529.
[5] Q. Liu, B. Guo, P. Chen, H. Zhai, Y. Guo, S. Tang, Experimental investigation blast resistance of CFRP/polyurea composite plates under blast loading, Thin-Walled Struct. 181 (2022) 110149.
[6] Q. Liu, B. Guo, P. Chen, J. Su, A. Arab, G. Ding, G. Yan, H. Jiang, F. Guo, Investigating ballistic resistance of CFRP/polyurea composite plates subjected to ballistic impact, Thin-Walled Struct. 166 (2021) 108111.
[7] T. Zhang, W. Cai, F. Chu, F. Zhou, S. Liang, C. Ma, Y. Hu, Hydroxyapatite/polyurea nanocomposite: Preparation and multiple performance enhancements, Composites A 128 (2020) 105681.
[8] S. Bordbar, M. Rezaeizadeh, A. Kavian, Improving thermal conductivity and corrosion resistance of polyurea coating on internal tubes of gas heater by nano silver, Prog. Org. Coat. 146 (2020) 105722.
[9] H. Yu, Z. He, G. Qian, X. Gong, X. Qu, Research on the anti-icing properties of silicone modified polyurea coatings (SMPC) for asphalt pavement, Constr. Build. Mater. 242 (2020) 117793.
[10] M. Song, Graphene functionalization and its application to polymer composite materials, Nanomater. Energy 2 (2013) 97–111.
[11] R.K.L. Tan, S.P. Reeves, N. Hashemi, D.G. Thomas, E. Kavak, R. Montazami, N.N. Hashemi, Graphene as a flexible electrode: review of fabrication approaches, J. Mater. Chem. A 5 (34) (2017) 17777–17803.
[12] Y. Yu, Q. Meng, T. Liu, Multifunctional and durable graphene-based composite sponge doped with antimonene nanosheets, J. Mater. Res. Technol. 17 (2022) 2466–2479.
[13] Z.-H. Zhang, Z.-Y. Chen, Y.-H. Tang, Y.-T. Li, D. Ma, G.-D. Zhang, R. Boukherroub, C.-F. Cao, L.-X. Gong, P. Song, K. Cao, L.-C. Tang, Silicone/graphene oxide co-cross-linked aerogels with wide-temperature mechanical flexibility, superhydrophobicity and flame resistance for exceptional thermal insulation and oil/water separation, J. Mater. Sci. Technol. 114 (2022) 131–142.
[14] S. Wang, M. Cao, H. Xue, S. Araby, F. Abbassi, Y. He, W. Su, Q. Meng, Investigation on graphene addition on the quasi-static and dynamic responses of carbon fibre-reinforced metal laminates, Thin-Walled Struct. 174 (2022) 109092.
[15] L.-Z. Guan, Y.-J. Wan, L.-X. Gong, D. Yan, L.-C. Tang, L.-B. Wu, J.-X. Jiang, G.-Q. Lai, Toward effective and tunable interphases in graphene oxide/epoxy composites by grafting different chain lengths of polyetheramine onto graphene oxide, J. Mater. Chem. A 2 (36) (2014) 15058–15069.
[16] Y. Yang, J.-R. Tao, D. Yang, Q.-M. He, X.-D. Chen, M. Wang, Improving dispersion and delamination of graphite in biodegradable starch materials via constructing cation-π interaction: Towards microwave shielding enhancement, J. Mater. Sci. Technol. 129 (2022) 196–205.
[17] J. Li, Y. Wang, T.-N. Yue, Y.-N. Gao, Y.-D. Shi, J.-B. Shen, H. Wu, M. Wang, Robust electromagnetic interference shielding, joule heating, thermal conductivity, and anti-dripping performances of polyoxymethylene with uniform distribution and high content of carbon-based nanofillers, Compos. Sci. Technol. 206 (2021) 108681.
[18] B.-F. Guo, P.-H. Wang, C.-F. Cao, Z.-H. Qu, L.-Y. Lv, G.-D. Zhang, L.-X. Gong, P. Song, J.-F. Gao, Y.-W. Mai, L.-C. Tang, Restricted assembly of ultralow loading of graphene oxide for lightweight, mechanically flexible and flame retardant polydimethylsiloxane foam composites, Composites B 247 (2022) 110290.
[19] M. Hernández, M. Bernal, A. Grande, N. Zhong, S. Zwaag, S. García, Effect of graphene content on the restoration of mechanical, electrical and thermal functionalities of a self-healing natural rubber, Smart Mater. Struct. 26 (2017) 085010.
[20] S. Guo, J. Chen, Y. Zhang, J. Liu, Graphene-based films: Fabrication, interfacial modification, and applications, Nanomaterials 11 (10) (2021) 2539.
[21] M.-H. Wang, Q. Li, X. Li, Y. Liu, L.-Z. Fan, Effect of oxygen-containing functional groups in epoxy/reduced graphene oxide composite coatings on corrosion protection and antimicrobial properties, Appl. Surf. Sci. 448 (2018) 351–361.
[22] W. Yu, L. Sisi, Y. Haiyan, L. Jie, Progress in the functional modification of graphene/graphene oxide: a review, RSC Adv. 10 (26) (2020) 15328–15345.
[23] A. Anwar, X. Liu, L. Zhang, Nano-cementitious composites modified with Graphene Oxide – a review, Thin-Walled Struct. 183 (2023) 110326.
[24] L.-B. Zhang, J. Wang, H.-G. Wang, Y. Xu, Z. Wang, Z. Li, Y.-J. Mi, S.-R. Yang, Preparation, mechanical and thermal properties of functionalized graphene/polyimide nanocomposites, Composites A 43 (2012) 1537–1545.
[25] H.J. Salavagione, Promising alternative routes for graphene production and functionalization, J. Mater. Chem. A 2 (20) (2014) 7138–7146.
[26] M. Yi, Z. Shen, A review on mechanical exfoliation for the scalable production of graphene, J. Mater. Chem. A 3 (22) (2015) 11700–11715.
[27] W. Zhao, M. Fang, F. Wu, H. Wu, L. Wang, G. Chen, Preparation of graphene by exfoliation of graphite using wet ball milling, J. Mater. Chem. 20 (2010) 5817.
[28] G. Shi, A. Michelmore, J. Jin, L.H. Li, Y. Chen, L. Wang, H. Yu, G. Wallace, S. Gambhir, S. Zhu, P. Hojati-Talemi, J. Ma, Advancement in liquid exfoliation of graphite through simultaneously oxidizing and ultrasonicating, J. Mater. Chem. A 2 (47) (2014) 20382–20392.
[29] J. Coleman, Liquid-phase exfoliation of nanotubes and graphene, Adv. Funct. Mater. 19 (2009) 3680–3695.
[30] Q. Meng, F. Meng, Y. Yu, J. Alam, S. Han, S. Chen, J. Ma, Preparation of antimonene nanosheets and their thermoelectric nanocomposites, Compos. Commun. 28 (2021) 100968.
[31] W. Du, X. Jiang, L. Zhu, From graphite to graphene: direct liquid-phase exfoliation of graphite to produce single- and few-layered pristine graphene, J. Mater. Chem. A 1 (36) (2013) 10592–10606.
[32] Q. Meng, G. Guo, X. Qin, Y. Zhang, X. Wang, L. Zhang, Smart multifunctional elastomeric nanocomposite materials containing graphene nanoplatelets, Smart Mater. Manuf. (2022) 100006.

[33] J.-M. Seo, I.-Y. Jeon, J.-B. Baek, Mechanochemically driven solid-state Diels–Alder reaction of graphite into graphene nanoplatelets, Chem. Sci. 4 (11) (2013) 4273–4277.
[34] U. Saha, R. Jaiswal, J.P. Singh, T.H. Goswami, Diisocyanate modified graphene oxide network structure: steric effect of diisocyanates on bimolecular cross-linking degree, J. Nanopart. Res. 16 (5) (2014) 2404.
[35] F.K. Urakaev, V.V. Boldyrev, Mechanism and kinetics of mechanochemical processes in comminuting devices: 1. Theory, Powder Technol. 107 (1) (2000) 93–107.
[36] S. Stankovich, R.D. Piner, S.T. Nguyen, R.S. Ruoff, Synthesis and exfoliation of isocyanate-treated graphene oxide nanoplatelets, Carbon 44 (15) (2006) 3342–3347.
[37] F. Zheng, P. Jiang, L. Hu, Y. Bao, J. Xia, Functionalization of graphene oxide with different diisocyanates and their use as a reinforcement in waterborne polyurethane composites, J. Macromol. Sci. A 56 (2019) 1071–1081.
[38] Y. Li, H. Tian, J. Zhang, W. Zou, H. Wang, Z. Du, C. Zhang, Fabrication and properties of rigid polyurethane nanocomposite foams with functional isocyanate modified graphene oxide, Polym. Compos. 41 (2020) 5126–5134.
[39] K. Holzworth, Z. Jia, A.V. Amirkhizi, J. Qiao, S. Nemat-Nasser, Effect of isocyanate content on thermal and mechanical properties of polyurea, Polymer 54 (12) (2013) 3079–3085.
[40] J.T. Garrett, R. Xu, J. Cho, J. Runt, Phase separation of diamine chain-extended poly(urethane) copolymers: FTIR spectroscopy and phase transitions, Polymer 44 (9) (2003) 2711–2719.
[41] X. Qian, B. Yu, C. Bao, L. Song, B. Wang, W. Xing, Y. Hu, R.K.K. Yuen, Silicon nanoparticle decorated graphene composites: preparation and their reinforcement on the fire safety and mechanical properties of polyurea, J. Mater. Chem. A 1 (34) (2013) 9827–9836.
[42] W. Lee, S.J. Howard, W.J. Clegg, Growth of interface defects and its effect on crack deflection and toughening criteria, Acta Mater. 44 (10) (1996) 3905–3922.
[43] P. Song, Z. Cao, Y. Cai, L. Zhao, Z. Fang, S. Fu, Fabrication of exfoliated graphene-based polypropylene nanocomposites with enhanced mechanical and thermal properties, Polymer 52 (18) (2011) 4001–4010.
[44] L. Jiang, Y. Lei, Y. Xiao, X. Fu, W. Kong, Y. Wang, J. Lei, Mechanically, robust, exceptionally recyclable and shape memory cross-linked network based on reversible dynamic urea bonds, J. Mater. Chem. A 8 (42) (2020) 22369–22378.
[45] J. Chen, F. Li, Y. Luo, Y. Shi, X. Ma, M. Zhang, D.W. Boukhvalov, Z. Luo, A self-healing elastomer based on an intrinsic non-covalent cross-linking mechanism, J. Mater. Chem. A 7 (25) (2019) 15207–15214.
[46] Z. Wang, M. Yang, X. Wang, G. Fei, Z. Zheng, H. Xia, NIR driven fast macro-damage repair and shear-free reprocessing of thermoset elastomers via dynamic covalent urea bonds, J. Mater. Chem. A 8 (47) (2020) 25047–25052.
[47] Z. Wang, S. Gangarapu, J. Escorihuela, G. Fei, H. Zuilhof, H. Xia, Dynamic covalent urea bonds and their potential for development of self-healing polymer materials, J. Mater. Chem. A 7 (26) (2019) 15933–15943.
[48] R. Wool, K. Oconnor, Crack healing in polymers, J. Appl. Phys. 52 (1981) 5953–5963.
[49] L. Xia, H. Tu, W. Zeng, X. Yang, M. Zhou, L. Li, X. Guo, A room-temperature self-healing elastomer with ultra-high strength and toughness fabricated via optimized hierarchical hydrogen-bonding interactions, J. Mater. Chem. A 10 (8) (2022) 4344–4354.
[50] J. Li, G. Zhang, L. Deng, S. Zhao, Y. Gao, J. Kun, R. Sun, C.P. Wong, In situ polymerization and mechanical reinforced, thermal healable graphene oxide/polyurethane composites based on diels–alder chemistry, J. Mater. Chem. A 2 (2014) 20642–20649.
[51] X. Luo, Y. Wu, M. Guo, X. Yang, L. Xie, J. Lai, Z. Li, H. Zhou, Multi-functional polyurethane composites with self-healing and shape memory properties enhanced by graphene oxide, J. Appl. Polym. Sci. 138 (2021) 50827.
[52] A.M. Grande, R. Martin, I. Odriozola, S. van der Zwaag, S.J. Garcia, Effect of the polymer structure on the viscoelastic and interfacial healing behaviour of poly(urea-urethane) networks containing aromatic disulphides, Eur. Polym. J. 97 (2017) 120–128.
[53] R.D. Zallen, C.M. Penchina, The physics of amorphous solids, Am. J. Phys. 54 (1986) 862–863.
[54] Y. Fu, J. Hansson, Y. Liu, S. Chen, A. Zehri, M.K. Samani, N. Wang, Y. Ni, Y. Zhang, Z.-B. Zhang, Q. Wang, M. Li, H. Lu, M. Sledzinska, C.M.S. Torres, S. Volz, A.A. Balandin, X. Xu, J. Liu, Graphene related materials for thermal management, 2D Mater. 7 (1) (2019) 012001.
[55] Y. Wen, C. Chen, Y. Ye, Z. Xue, H. Liu, X. Zhou, Y. Zhang, D. Li, X. Xie, Y.-W. Mai, Advances on thermal conductive epoxy-based composites as electronic packaging underfill materials – A review, Adv. Mater. (2022) 2201023.
[56] G. Huang, W. Chen, T. Wu, H. Guo, C. Fu, Y. Xue, K. Wang, P. Song, Multifunctional graphene-based nano-additives toward high-performance polymer nanocomposites with enhanced mechanical, thermal, flame retardancy and smoke suppressive properties, Chem. Eng. J. 410 (2021) 127590.
[57] Q. Gao, Y. Pan, G. Zheng, C. Liu, C. Shen, X. Liú, Flexible multilayered mxene/thermoplastic polyurethane films with excellent electromagnetic interference shielding, thermal conductivity, and management performances, Adv. Compos. Hybrid Mater. 4 (2021) 274–285.
[58] S. Kang, T.-H. Kang, B. Kim, J. Oh, S. Park, I. Choi, J. Lee, J. Son, 2D reentrant micro-honeycomb structure of graphene-CNT in polyurethane: High stretchability, superior electrical/thermal conductivity, and improved shape memory properties, Composites B 162 (2019) 580–588.
[59] Z. Zhu, C. Li, E. Songfeng, L. Xie, R. Geng, C.-T. Lin, L. Li, Y. Yao, Enhanced thermal conductivity of polyurethane composites via engineering small/large sizes interconnected boron nitride nanosheets, Compos. Sci. Technol. 170 (2019) 93–100.
[60] Y.-C. Soong, C.-W. Chiu, Multilayered graphene/boron nitride/thermoplastic polyurethane composite films with high thermal conductivity, stretchability, and washability for adjustable-cooling smart clothes, J. Colloid Interface Sci. 599 (2021) 611–619.
[61] G. Xiao, J. Di, H. Li, J. Wang, Highly thermally conductive, ductile biomimetic boron nitride/aramid nanofiber composite film, Compos. Sci. Technol. 189 (2020) 108021.
[62] T. Fei, Y. Li, B. Liu, C. Xia, Flexible polyurethane/boron nitride composites with enhanced thermal conductivity, High Perform. Polym. 32 (3) (2019) 324–333.
[63] C. Yu, W. Gong, W. Tian, Q. Zhang, Y. Xu, Z. Lin, M. Hu, X. Fan, Y. Yao, Hot-pressing induced alignment of boron nitride in polyurethane for composite films with thermal conductivity over 50 Wm -1 k -1, Compos. Sci. Technol. 160 (2018) 199–207.
[64] S. Han, Q. Meng, Z. Qiu, A. Osman, R. Cai, Y. Yu, T. Liu, S. Araby, Mechanical, toughness and thermal properties of 2D material- reinforced epoxy composites, Polymer 184 (2019) 121884.
[65] J.H. Seol, I. Jo, A.L. Moore, L. Lindsay, Z.H. Aitken, M.T. Pettes, X. Li, Z. Yao, R. Huang, D. Broido, N. Mingo, R.S. Ruoff, L. Shi, Two-dimensional phonon transport in supported graphene, Science 328 (5975) (2010) 213–216.
[66] T. Ouyang, Y. Chen, Y. Xie, K. Yang, Z. Bao, J. Zhong, Thermal transport in hexagonal boron nitride nanoribbons, Nanotechnology 21 (24) (2010) 245701.
[67] E. Pop, D. Mann, Q. Wang, K. Goodson, H. Dai, Thermal conductance of an individual single-wall carbon nanotube above room temperature, Nano Lett. 6 (1) (2006) 96–100.
[68] J. Hone, M.C. Llaguno, M.J. Biercuk, A.T. Johnson, B. Batlogg, Z. Benes, J.E. Fischer, Thermal properties of carbon nanotubes and nanotube-based materials, Appl. Phys. A 74 (3) (2002) 339–343.
[69] X.-H. Zha, J. Zhou, Y. Zhou, Q. Huang, J. He, J.S. Francisco, K. Luo, S. Du, Promising electron mobility and high thermal conductivity in Sc2CT2 (T = F, OH) MXenes, Nanoscale 8 (11) (2016) 6110–6117.
[70] M. Wang, Y. Liu, H. Zhang, Y. Wu, L. Pan, Thermal conductivities of ti3c2tx mxenes and their interfacial thermal performance in mxene/epoxy composites – a molecular dynamics simulation, Int. J. Heat Mass Transfer 194 (2022) 123027.
[71] H. He, L. Guan, H. Le Ferrand, Controlled local orientation of 2D nanomaterials in 3D devices: methods and prospects for multifunctional designs and enhanced performance, J. Mater. Chem. A 10 (37) (2022) 19129–19168.
[72] H. Hou, W. Dai, Q. Yan, L. Lv, F.E. Alam, M. Yang, Y. Yao, X. Zeng, J.-B. Xu, J. Yu, N. Jiang, C.-T. Lin, Graphene size-dependent modulation of graphene frameworks contributing to the superior thermal conductivity of epoxy composites, J. Mater. Chem. A 6 (25) (2018) 12091–12097.